

Atmospheric and surface adjacency effects modeled by the radiosity method

Christoph.C. Borel
 Ball Aerospace & Technologies Corp.
 2875 Presidential Drive, Suite 180
 Fairborn, Ohio 45324-6269
 Email: cborel@ball.com

Abstract

Most commonly used atmospheric correction methods for remotely sensed data take absorption and scattering by gases and aerosols into account (ACORNTM [1], HATCHTM [11]). However when retrieving reflectances for a remotely sensed image the atmospheric and surface adjacency effect must be considered. Only a few atmospheric correction methods also correct for the atmospheric adjacency (FLAASH [2], ATCORTM [21]) and perform a terrain correction for the illumination (ATCOR).

The atmospheric adjacency effect is due to scattering of light from bright neighboring surfaces into the line of sight, thus, it tends to somewhat blur the image and mix spectra from other surfaces. It has been modeled successfully using Monte Carlo calculations. We present an update to a conceptually simpler numerical technique based on the radiosity method and show how it depends on the aerosol scattering phase function, height distribution, and surface BRDF.

It is very difficult to correct for the surface adjacency effect where light is incident on a surface not only by direct illumination of the sun but also from nearby objects such as trees, buildings, and mountain slopes. Reflections between adjacent objects can change the apparent reflectance of a pixel significantly and thus make classification more difficult. We present several simulations based on radiosity calculations to illustrate the surface adjacency effect.

I. INTRODUCTION

The adjacency-blurring-effect is observed at the boundary between a dark and a bright surface. Near the edge over a dark surface, photons from the nearby bright surface may be scattered within the atmosphere into the field of view (FOV) of an airborne or satellite sensor. Conversely, near the edge over a bright surface, fewer photons reach the sensor's FOV. At a sharp discontinuity in the surface reflectance, the intensity transect appears as a sigmoid instead of a step function. Figure 1 shows the paths the photons take from nearby surfaces to scatter into the line of sight. The adjacency-blurring-effect may introduce errors in the detection and classification of small bright targets surrounded by a dark region or dark targets on a bright background. One can model the blurring due to the adjacency effect with a point spread function (PSF). This PSF is a filter function that is convolved with the unperturbed (no atmosphere) reflectance image of a surface. Some papers discussing the adjacency effect are in references [24], [23], [14], [10], [3], [20], [19], [4], [17], [9]. Most PSF's are generated by Monte Carlo based methods and are assumed to be rotationally symmetric, thus, they are not valid for off-nadir views. In the situation of an oblique viewing sensor, it is necessary to compute off-nadir PSF's, which are generally asymmetric.

The spatial adjacency effect occurs when the total irradiance E_{total} has significant contributions from neighboring surfaces, i.e. $E_{total} \leq E_{direct}$, where E_{direct} is the direct irradiance. Thus, the reflection coefficient $\rho_{surface}$ of a surface can no longer be estimated as:

$$\rho_{surface} = \frac{L_{measured} - L_{path}}{E_{direct}\tau}, \quad (1)$$

where $L_{measured}$ is the measured surface radiance, L_{path} is the path radiance, and τ is the transmission from the sun through the atmosphere to the ground and back to the sensor. In Figure 2 the total irradiance components are shown and their scattering paths.

In [17] the total irradiance E_{total} is given as:

$$E_{total} = E_{direct} + E_{diffuse} + E_{coupling} + E_{direct-reflected} + E_{diffuse-reflected}, \quad (2)$$

where direct irradiance at a point P is given as:

$$E_{direct} = E_{TOA} \langle \hat{n}(P) \cdot \hat{n}_s \rangle \tau_{sun-ground},$$

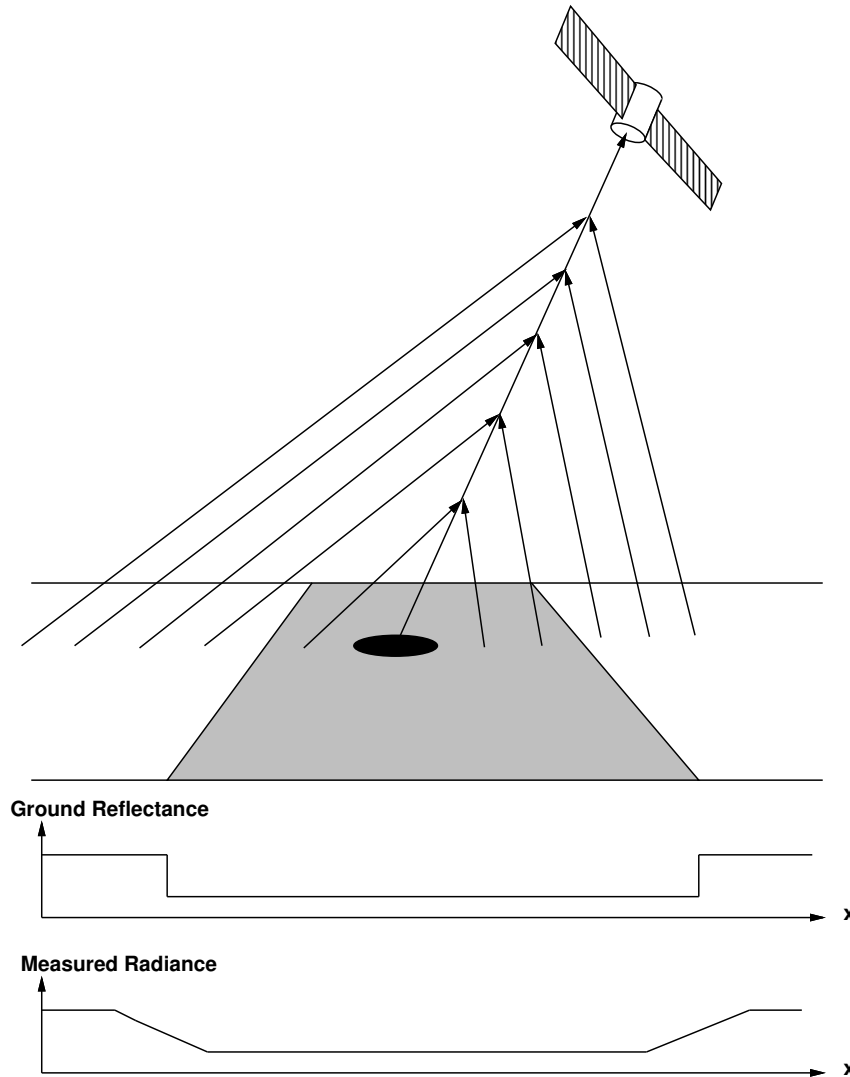


Fig. 1. The adjacency effect occurs due to scattering of photons into the line of sight from surrounding brighter surfaces.

where E_{TOA} is the top-of-atmosphere irradiance, $\hat{n}(P)$ is the surface normal vector, and \hat{n}_s is the vector to the sun. Most atmospheric correction codes assume the surface normal is aligned with the zenith direction, and others require a digital elevation model to be registered with the sensor data, which is often a difficult task. For shaded areas where $E_{direct} = 0$, the irradiance is dependent on all the other terms in (2), thus making it important to model the additional irradiance terms that are usually an order of magnitude smaller than the direct term.

The diffuse irradiance, $E_{diffuse}$, is due to diffuse radiance coming from the sky E_{sky} . A very simple approximation ($E_{sky} = \text{const}$) is given in [26] as:

$$E_{diffuse} = E_{sky} \frac{1 + \langle \hat{n}(P) \cdot \hat{n}_s \rangle}{2}.$$

Computations using atmospheric transmission codes such as MODTRANTM [5] show the sky radiance is significant in the visible but decreases in the near infrared.

The coupling irradiance is very difficult to model. Tanré [23] describes it as a second scattered flux that is due to successive reflections and scattering between the surface and the atmosphere. The coupling irradiance [17] can be written using the spherical albedo of the atmosphere S as:

$$E_{coupling} = \frac{E_{direct}\tau_{direct} + E_{diffuse}\tau_{diffuse}}{1 - \langle \rho \rangle S},$$

where $\langle \rho \rangle$ is a spatial average of the reflectance near point P . Typical values for the scattering albedo range from 5% to 10% in the visible, less than 3% in the near infrared, and less than 1% in the SWIR. The scattering albedo S is directly

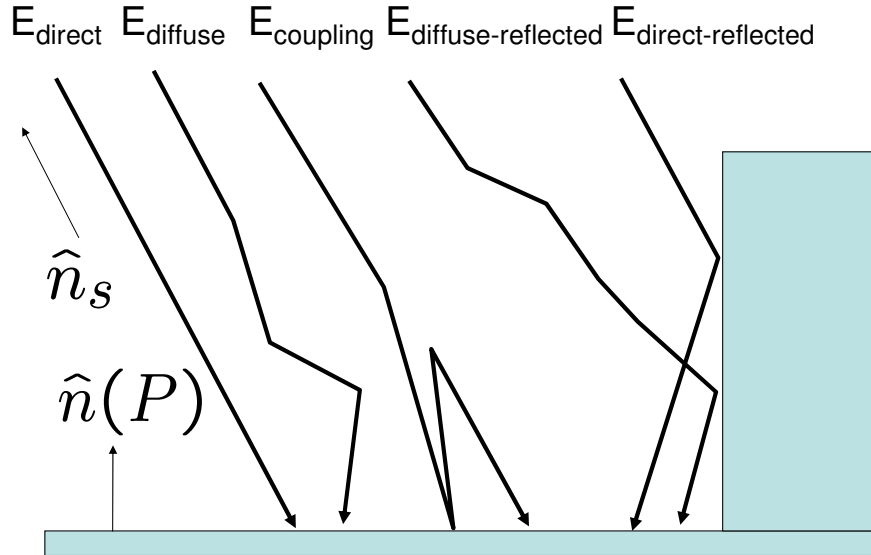


Fig. 2. Irradiance contributions for a point P on the ground.

computed in 6S and can be derived by a series of runs with different surface albedos using MODTRAN [16].

The next two terms in (2) result from either direct irradiance E_{direct} or diffuse irradiance $E_{diffuse}$ reflected from an adjacent slope point M to point P weighted by the attenuation due to scattering and absorption. The difficulty in computing this term is to decide how far to go for the integration, one paper [17] suggests a couple of km.

We introduce now a method to compute the atmospheric and surface adjacency effect. The method is based on the extended radiosity method [6]. The extended radiosity method (sometimes called the "Zonal method") is a natural way to compute the sensor radiance without having to resort to complex nomenclature such as in [17] to derive terms that, in the end, are not really of interest. Thus, we will start with a summary of the extended radiosity method and then derive the adjacency point spread function for any view direction and any layered atmosphere that includes scattering phase functions. We will then give the equations for a simple wedge model, which is useful to understand the effect of multiple reflections on the spectral shape.

II. EXTENDED RADIOSITY METHOD

A. Equations

The extended radiosity method for illuminated surfaces A_i and volume elements V_k is based on the two following coupled linear systems of equations for monochromatic radiation [13], [22]:

$$B_i^s A_i = E_i^s A_i + \rho_i \left[\sum_{j=1}^{N_s} B_j^s \underline{S_j S_i} + \sum_{k=1}^{N_v} B_k^v \underline{V_k S_i} \right], \quad i = 1, \dots, N_s, \quad (3)$$

$$4 \kappa_{t,k} B_k^v V_k = 4 \kappa_{a,k} E_k^v V_k + \alpha_k \left[\sum_{j=1}^{N_s} B_j^s \underline{S_j V_k} + \sum_{m=1}^{N_v} B_m^v \underline{V_m V_k} \right], \quad k = 1, \dots, N_v, \quad (4)$$

where B_i^s is the surface radiosity in $[W m^{-2}]$, E_i^s is the emission, and ρ_i is the reflectance of surface patch i with area A_i . The flux density leaving a volume element k is given by $4 \kappa_{t,k} B_k^v V_k$ where $\kappa_{t,k}$ is the sum of the absorption coefficient

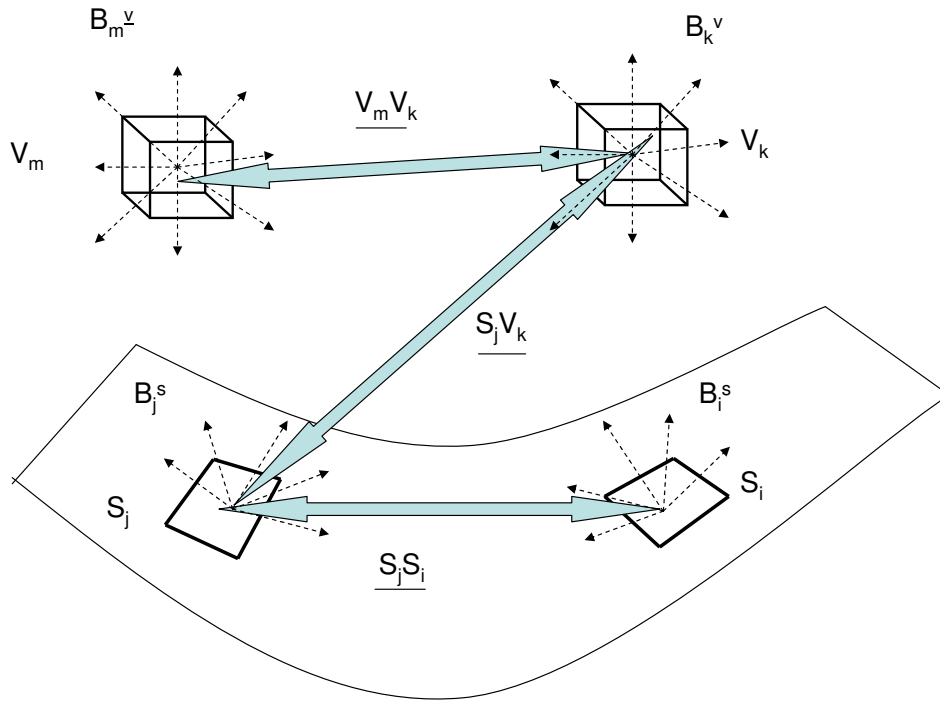


Fig. 3. Extended radiosity model or zonal method for radiative exchanges between volumes, volumes and surfaces and surfaces.

$\kappa_{a,k}$ and the scattering coefficient $\kappa_{s,k}$, and B_k^v is the volume radiosity. The scattering albedo of the k -th volume element is $\alpha_k = \kappa_{s,k}/\kappa_{t,k}$. The volume and surface radiosities are given by the sums of its emission and the scattered and reflected radiosities from all other surfaces and volumes. The fraction of energy reaching a surface or volume from another surface or volume through an absorbing medium is given by view factors. The view factor from a surface k to surface j is $\underline{S_k S_j}$, the view factor from volume k to surface i is $\underline{V_k S_i}$, the view factor from surface j to volume k is $\underline{S_j V_k}$, and the view factor from volume m to volume k is $\underline{V_m V_k}$. The view factors depend on the geometry and attenuation of fluxes between elements and are usually difficult to evaluate. Finally we note that there are N_s surface elements with indices i or j and N_v volume elements with indices k and m . In Figure 3, we show the volume and surface elements and the viewfactors between them. Eqs. (3) and (4) assume the surfaces are Lambertian reflectors so light is scattered equally into all directions. Three-dimensional structures like clouds, fog, and smoke can be simulated by assigning absorption and scattering characteristics independently for each volume element V_k .

The view factor from surface i to surface j is defined as [13], [22]:

$$\underline{S_i S_j} = \int_{A_k} \int_{A_j} \frac{dA_i \cos \theta_i dA_j \cos \theta_j \tau(r)}{\pi r^2}. \tag{5}$$

The view factor from volume k to surface i is defined as [13], [22]:

$$\underline{V_k S_i} = \int_{V_k} \int_{A_i} \frac{\kappa_{t,k} dV_k dA_i \cos \theta_i \tau(r)}{\pi r^2}. \tag{6}$$

The view factor between volume m and volume k is defined as [13], [22] :

$$\underline{V_m V_k} = \int_{V_k} \int_{V_m} \frac{\kappa_{t,m} dV_m \kappa_{t,k} dV_k \tau(r)}{\pi r^2}. \tag{7}$$

The transmittance τ is given by :

$$\tau(r) = \exp \left[- \int_0^r \kappa_t(\chi) d\chi \right] \quad (8)$$

for a medium with variable κ_t along the line-of-sight path of length r .

B. Solution of the radiosity equations

The solution of eqs. (3,4) using eqs. (5-7) can be obtained using the Gauss-Seidel iteration scheme [18]. The following two eqs. show the mechanism:

$$B_i^{s,l+1} = E_i^s + \frac{\rho_i}{A_i} \sum_{k=1}^{N_v} B_k^{v,n} \underline{V_k S_i} - \frac{\rho_i}{A_i} \left[\sum_{j=1}^{i-1} B_j^{s,l+1} \underline{S_j S_i} + \sum_{j=i+1}^{N_s} B_j^{s,l} \underline{S_j S_i} \right], \quad i = 1, \dots, N_s \quad (9)$$

$$B_k^{v,n+1} = \frac{\kappa_{a,k}}{\kappa_{t,k}} E_k^v + \frac{\alpha_k}{4 \kappa_{t,k} V_k} \sum_{j=1}^{N_s} B_j^{s,l+1} \underline{S_j V_k} - \frac{\alpha_k}{4 \kappa_{t,k} V_k} \left[\sum_{j=1}^{k-1} B_j^{v,n+1} \underline{V_j V_k} + \sum_{j=k+1}^{N_v} B_j^{v,n} \underline{V_j V_k} \right], \quad k = 1, \dots, N_v \quad (10)$$

The superscripts l and n denote the iteration. The iteration ends when the absolute errors for the surface and volume radiosities fulfill the following criteria:

$$\frac{|B_i^{s,l+1} - B_i^{s,l}|}{B_i^{s,l}} < \varepsilon \text{ for all } i = 1, \dots, N_s \quad (11)$$

and

$$\frac{|B_k^{v,n+1} - B_k^{v,n}|}{B_k^{v,n}} < \varepsilon \text{ for all } k = 1, \dots, N_v. \quad (12)$$

The number of required iterations varies between 10 and 30 for most cases with an error limit of $\varepsilon = 10^{-9}$.

C. Rendering a scene

The computed radiosities using eqs. (9) and (10) must be processed further to produce an image of the scene. The quantity a sensor measures is the radiance I that has units of Watts per area per unit solid angle (e.g., $W m^{-2} sr^{-1}$). One can show for Lambertian surfaces, the radiance is equal to the radiosity divided by π (e.g., [6]). The radiance from a surface behind a participating medium is attenuated by the transmission τ . The participating medium contributes additional radiance into the line of sight, with closer volume elements contributing more than more distant volume elements. The intensity of the light reaching the observer from a certain direction or along a ray is given by [22]:

$$I(L) = \tau(L) \frac{B_i^s}{\pi} + \int_0^L \tau(l) \frac{B^v(l)}{\pi} \kappa_t(l) dl, \quad (13)$$

$I(L)$ is the intensity on the outside of the imaged parallelepiped, L is the distance between the entrance point of a ray to the exit point at the detector location. If the exit point lies on the surface, the attenuated radiosity B_i^s must be added to the integral. The volume radiosity $B^v(l)$ along a ray from 0 to L can be approximated by a trilinear interpolation of the discrete volume radiosities. In the next sections we derive a point spread function using the radiosity view factors as a way to compute the scattering between the surface into the line of sight.

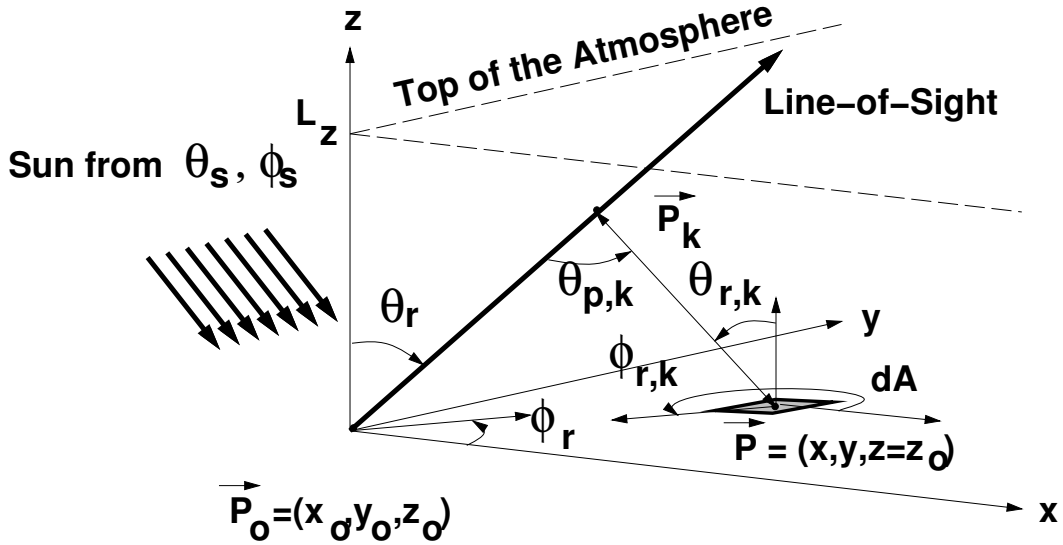


Fig. 4. Geometry for computing the point spread function.

III. COMPUTING THE POINT SPREAD FUNCTION FOR LAMBERTIAN SURFACES

In an optical system, the point spread function $PSF(x, y, z; x_0, y_0, z_0; \theta_s, \phi_s; \theta_r, \phi_r)$ can be defined as the scattering contribution of a surface element $dA = dx dy$ illuminated from direction (θ_s, ϕ_s) located at $(x, y, z = z_0)$ into the line-of-sight direction of the observer (θ_r, ϕ_r) looking at point (x_0, y_0, z_0) . Figure 4 shows the geometry for the ground to atmosphere scattering. One can show (see [7]) the unitless PSF is given by:

$$PSF(x, y) = \frac{\kappa_s \Delta l}{4 \pi} \sum_{k=1}^K \frac{\tau(r_k) \cos \theta_{r,k} f(\theta_{p,k}) dx dy}{\pi r_k^2} \cdot \exp(-\kappa_t (K - k) \Delta l), \quad (14)$$

where κ_s is the scattering coefficient in $[m^{-1}]$, $\Delta l = L_z / (K \cos \theta_r)$, L_z is the height of the scattering atmosphere, K is the number of layers in the atmosphere, $\tau(r_k) = \exp(-\kappa_t r_k)$, κ_t is the total scattering coefficient in $[m^{-1}]$, r_k is the distance between surface point \vec{P} and a point \vec{P}_k on the line-of-sight in the k -th layer, $\theta_{r,k}$ is the view zenith angle to dA , $f(\theta_{p,k})$ is the scattering phase function of the k -th layer, and $\theta_{p,k}$ is the scattering phase angle. Note this method takes height dependent scattering and absorption coefficients and even height dependent scattering phase functions into account. The method can even be extended to include terrain effects when the PSF is computed for each pixel in the scene. For the Lambertian surface the PSF for nadir view is rotationally symmetric and asymmetric for all non-nadir views.

According to [7], the measured radiance $I_{measured}(x, y, z; x_0, y_0, z_0; \theta_s, \phi_s; \theta_r, \phi_r)$ in $[W m^{-2}]$ at the sensor for a Lambertian surface, is given by:

$$I_{measured}(x, y) = \frac{E_0}{\pi} \tau_s \left[\tau_r \rho(x_0, y_0) + \rho(x, y) \otimes PSF(x, y) \right] + I_{path} \quad (15)$$

where E_0 is the direct energy incident from the sun in $[W m^{-2}]$, $\tau_s = \exp(-\kappa_t L_z / \cos \theta_s)$, $\tau_r = \exp(-\kappa_t L_z / \cos \theta_r)$, $\rho(x, y)$ is the reflectance at point (x, y) , \otimes denotes the convolution, and I_{path} is the path radiance or radiance due to scattering in the atmosphere. Equation 15 only takes single scattering events from a surface element into the line of sight into account and “lumps” all multiple reflected terms into the path radiance. This approximation is necessary since it is not possible to solve the volume rendering radiosity equation 13 for this case since the scattering phase function is not uniform.

IV. THE POINT SPREAD FUNCTION FOR NON-LAMBERTIAN SURFACES

In practical situations, the imaged ground surface is non-Lambertian, and thus, the above-described method may lead to inaccurate simulated images. We attempt now to include the bidirectional reflectance distribution function (BRDF) in the computation of the PSF. First, let us assume the entire surface has the BRDF :

$$f(x, y, z; \theta_s, \phi_s; \theta_r, \phi_r) = f(\theta_s, \phi_s; \theta_r, \phi_r).$$

Second, the contributions from indirect skylight are negligible on the radiance in direction $(\theta_{r,k}, \phi_{r,k})$ or the upwelling radiance I_{ground} at the ground level is proportional to $f(\theta_s, \phi_s; \theta_r, \phi_r)$. This second assumption clearly is not valid for turbid atmospheres and for highly specular surfaces like water. Under these two assumptions, we can replace $\rho(x, y)$ in eq.(14) with $\pi f(\theta_s, \phi_s; \theta_r, \phi_r)$. Note BRDF's for natural surfaces are usually asymmetric and cause the PSF to be asymmetric for all view directions, including nadir. The PSF for non-Lambertian surfaces is then given by:

$$PSF(x, y) = \frac{\kappa_s \Delta l}{4 \pi} \sum_{k=1}^K \frac{\tau(r_k) f(\theta_s, \phi_s; \theta_{r,k}, \phi_{r,k}) \cos \theta_{r,k} f(\theta_{p,k}) dx dy}{r_k^2} \exp(-\kappa_t (K - k) \Delta l), \quad (16)$$

where $\phi_{r,k}$ is the view azimuth angle of surface dA from point \vec{P}_k .

V. SIMULATION OF SCENES WITH HETEROGENEOUS SURFACE COVER

The Earth's, surface is composed of a mosaic of various surface types such as vegetation, bare soil, and water, each with distinct BRDF's. To simulate an oblique view over a heterogeneous surface, the following algorithm was used:

- 1) For each surface BRDF $f_i(\theta_s, \phi_s; \theta_r, \phi_r)$, $i = 1, 2, \dots, N$ compute the point spread function $PSF_i(x, y)$ using eq (16).
- 2) Generate a binary image $Q_i(x, y)$ for each surface type i , where $Q_i(x, y) = 1$ if the point (x, y) has surface cover type i and 0 otherwise.
- 3) Convolve each image $Q_i(x, y)$ with its point spread function $PSF_i(x, y)$.

The measured radiance image is then given by:

$$I_{measured}(x, y) = \frac{E_0}{\pi} \tau_s \sum_{i=1}^N \left[\tau_r Q_i(x_0, y_0) f_i(\theta_s, \phi_s; \theta_r, \phi_r) + Q_i(x, y) \otimes PSF_i(x, y) \right] + I_{path}. \quad (17)$$

Equation (17) shows the adjacency blurring effect is the superposition of ground cover type images convolved with their corresponding point spread functions.

To illustrate the method on an example, we used scattering phase function and BRDF's found in the literature.

To approximate a "hazy" atmosphere, we used the Henyey-Greenstein phase function with the asymmetry factor $\Theta = 0.75$ [15]. The Henyey-Greenstein phase function is defined as:

$$f(\theta_p) = \frac{1 - \Theta^2}{(1 + \Theta^2 - 2\Theta \cos \theta_p)^{3/2}}. \quad (18)$$

We selected a $\kappa_t = 0.8$, $\kappa_a = 0.05$ for an aerosol laden atmosphere of 1000 m height with 20 layers and a surface of 3000 m by 3000 m horizontal extent with 30 by 30 pixels.

The BRDF of bare ground was taken from [12]:

$$f(\theta_s, \phi_s; \theta_r, \phi_r) = \frac{\omega}{4\pi} \frac{1}{\mu_s + \mu_r} \left[\{1 + B(g)\} P(g) + H(\mu_s) H(\mu_r) - 1 \right], \quad (19)$$

where ω is the average single scattering albedo, $\mu_s = \cos \theta_s$, $\mu_r = \cos \theta_r$, $\cos g = \mu_s \mu_r + \sin \theta_s \sin \theta_r \cos(\phi_r - \phi_s)$, $B(g) = B_0/[1+h^{-1} \tan(g/2)]$, $B_0 = S(0)/(\omega P(0))$, $P(g) = 1+b \cos g+c[(3 \cos^2 g-1)/2]$, and $H(x) = (1+2x)/(1+2[1-\omega]^{1/2} x)$. The BRDF parameters chosen were: $\omega = 0.57$, $S(0) = 0.48$, $h = 0.21$, $b = 0.86$ and $c = 0.7$. The BRDF of the vegetated surface was taken from a parametric model [25] with the same notation as above where not listed:

$$f(\theta_s, \phi_s; \theta_r, \phi_r) = \frac{\omega}{4\pi} \frac{\nu_s}{\nu_s \mu_s + \nu_r \mu_r} \left[P_v(g) P(g) + H\left(\frac{\mu_s}{\nu_s}\right) H\left(\frac{\mu_r}{\nu_r}\right) - 1 \right], \quad (20)$$

where ν_s and ν_r describe the leaf orientation distribution for the illumination and observation angles that depend on a parameter χ_l with range: $(-0.4 < \chi_l < 0.6)$, $P(g)$ is the leaf scattering phase function that is the Henyey-Greenstein function in eq (18), the function $P_v(g)$ depends on the variable $G = [\tan^2 \theta_s + \tan^2 \theta_r - 2 \tan \theta_s \tan \theta_r \cos(\phi_s - \phi_r)]^{1/2}$, the radius of sun flecks r in [m] and Λ the leaf area density in [$m^2 m^{-3}$]. We selected the following canopy parameters: $\omega = 0.8$, $\Theta = -0.4$, $\Lambda = 0.01$, $r = 1.$, $\chi_l = 0.2$.

For the water surface, we assumed the BRDF to be a Henyey-Greenstein phase function $f(\theta_s, \phi_s; \theta_r, \phi_r) = \rho_{water} P(g)$ with the forward peak aligned with the specular reflectance direction $(\theta_s, \phi_s + \pi)$ or $g = \cos^{-1}[\mu_s \mu_r + \sin \theta_s \sin \theta_r \cos(\phi_s - \phi_r - \pi)]$. We selected a reflectance ρ_{water} of 2.55 % and an asymmetry factor of $\Theta = 0.95$. Figure 5 shows the point spread functions for (a) bare soil, (b) vegetation, and (c) water. Note the PSF's are asymmetric, and the PSF for water has a ridge in the specular reflection direction (left side) of the sun, which has a zenith angle of 30° .

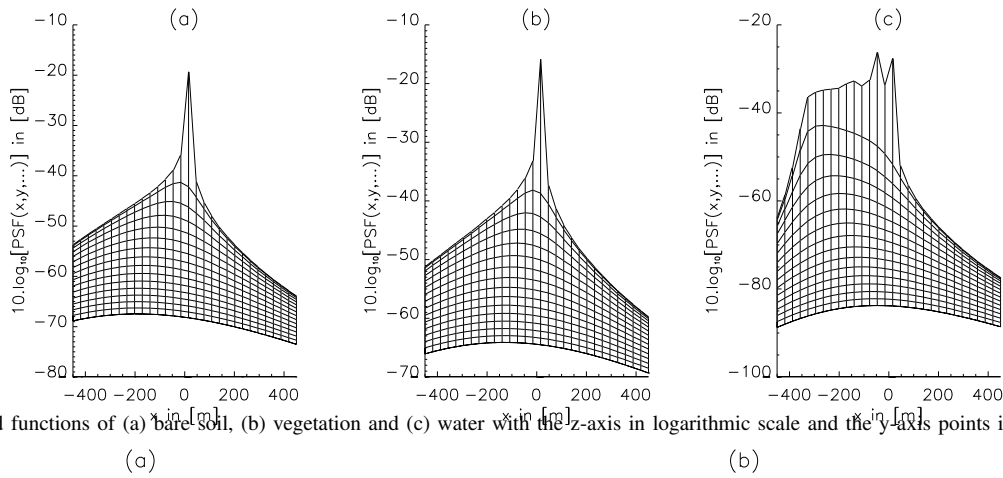


Fig. 5. Point spread functions of (a) bare soil, (b) vegetation and (c) water with the z-axis in logarithmic scale and the y-axis points into the paper.

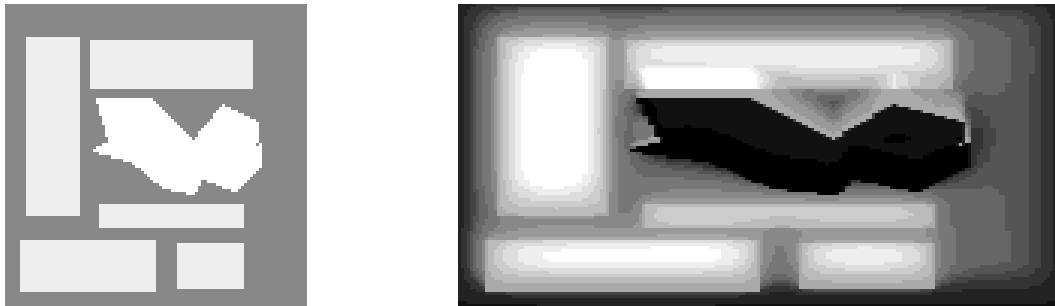


Fig. 6. Simulated scene from (a) above and (b) viewed through atmosphere from the below at 60° view zenith angle and illuminated from above at 30° sun zenith angle.

In Figure 6, we show a simulated scene containing some rectangular vegetated surfaces (light gray) surrounded by bare soil (dark gray) and a lake (black) in the middle. The simulated scene measures 3 km by 3 km and is viewed from below with a zenith angle of 60° . The sun light is incident from above with a zenith angle of 30° . To make faint radiance changes more visible, we show the histogram equalized radiance image. One can see the effect of the specular reflection of the sunlight into the atmosphere on the radiance in the field at the top of image (b). The edges of the fields closer to the observer appear darker than the edges away from the observer. Near the lower edge of the lake, the radiance decreases while it increases at the upper edge due to the increased scattering above the water surface.

VI. THE WEDGE MODEL

In [8], we describe a wedge model in the context of nonlinear mixing models. It is quite simple to expand the model to include arbitrary illumination and viewing angles. Using Hottel’s crossed string method, it is possible to compute view factors between the illuminated and shaded parts of the wedge and to write the radiosity equations. After the radiosities are computed using an iterative scheme, we compute the visibility of the facets from a given view direction and compute the bidirectional reflectance factor (BRF) that is given by the sum of the products of the radiosities times the visibility divided by the incident energy. The model is quite simple, but enables us to rapidly compute the effects of multiple scattering within a rough surface as a function of illumination and view direction. To keep the notation simple we restrict the illumination angle that is measured from the x axis to angles between 0 and $\frac{\pi}{2}$.

A. Wedge Geometry

The geometry of a wedge is shown in Figure 7. We note the points on the wedge are given by: $\vec{A} = (-w \cos \theta, w \sin \theta)$, $\vec{B} = (0, 0)$, $\vec{C} = (w \cos \theta, w \sin \theta)$, and the shadow point \vec{S} is given by: $\vec{S} = (\vec{A} - \vec{B})f_p$ where :

$$f_p = \begin{cases} \frac{\sin \theta \cos \theta_0 - \cos \theta \sin \theta_0}{\sin \theta} & 0 < \theta_0 < \theta \\ 0 & \theta < \theta_0 < \frac{\pi}{2} \end{cases} .$$

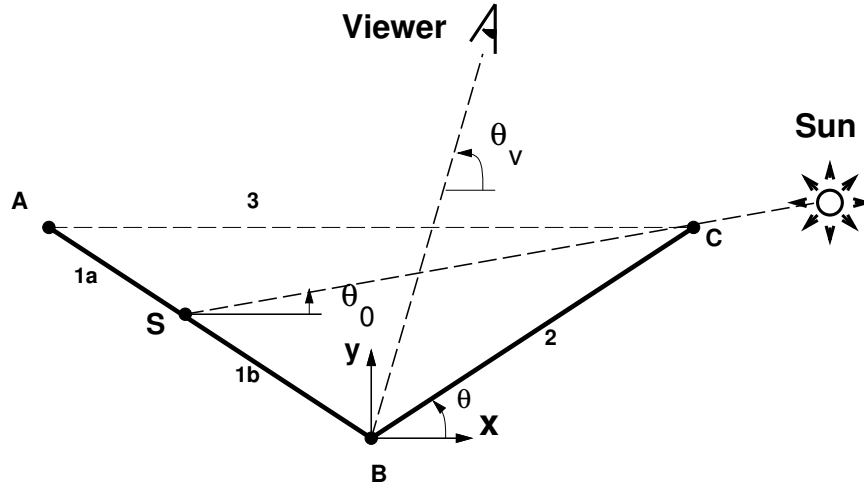


Fig. 7. Geometry of a wedge.

Thus, we are only considering illumination angles from $0 < \theta_0 < \frac{\pi}{2}$ so shadows can only occur on facet 1. The slope angle is θ , and the illumination angle θ_0 is measured from the horizon.

The distances between points or “string lengths” are given by:

$$\begin{aligned} \overline{AB} &= |\vec{A} - \vec{B}| = w, \\ \overline{BC} &= |\vec{B} - \vec{C}| = w, \\ \overline{AC} &= |\vec{A} - \vec{C}| = 2w \cos \theta, \\ \overline{AS} &= |\vec{A} - \vec{S}| = (1 - f_p)w, \\ \overline{BS} &= |\vec{B} - \vec{S}| = f_p w, \\ \overline{CS} &= |\vec{C} - \vec{S}|. \end{aligned}$$

B. View Factors

The view factors can be computed using Hottel’s crossed string method [13]. An example of the method is shown in Figure 8. The view factor between two infinite strips with areas S_1 and S_2 is given by :

$$S_1 F_{12} = \frac{\overline{AD} + \overline{BC} - \overline{AC} - \overline{BD}}{2},$$

where \overline{AD} is the length between the points A and D , etc.

We list now the view factors between all facets (1a, 1b, 2, and 3). Note view factors from and to facet 1b exist only if there is a shadow point \vec{S} :

$$\begin{aligned} F_{1a2} &= \frac{\overline{AB} + \overline{CS} - \overline{AC} - \overline{BS}}{2w(1 - f_p)}, \\ F_{1b2} &= \frac{\overline{BS} + \overline{BC} - \overline{CS}}{2w f_p}, \text{ if } \vec{S} \text{ exists,} \\ F_{21a} &= \frac{\overline{AB} + \overline{CS} - \overline{AC} - \overline{BS}}{2w}, \\ F_{21b} &= \frac{\overline{BC} + \overline{BS} - \overline{CS}}{2w}, \text{ if } \vec{S} \text{ exists,} \\ F_{1a3} &= \frac{\overline{AS} + \overline{AC} - \overline{CS}}{2w(1 - f_p)}, \end{aligned}$$

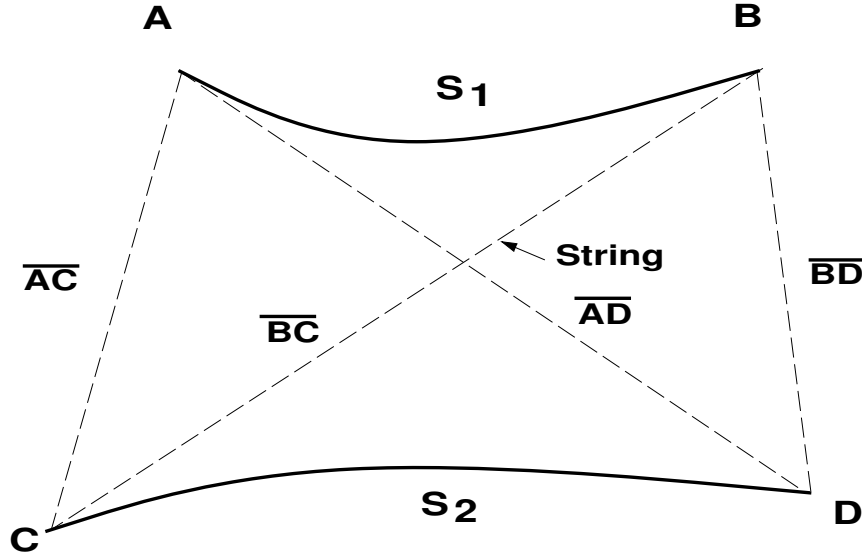


Fig. 8. Crossed string method to compute view factors.

$$F_{1b3} = \frac{\overline{AB} + \overline{CS} - \overline{AS} - \overline{BC}}{2w f_p}, \text{ if } \vec{S} \text{ exists,}$$

$$F_{31a} = \frac{\overline{AS} + \overline{AC} - \overline{CS}}{4w \cos \theta},$$

$$F_{31b} = \frac{\overline{AB} + \overline{CS} - \overline{AS} - \overline{BC}}{4w \cos \theta}, \text{ if } \vec{S} \text{ exists,}$$

$$F_{23} = \frac{\overline{BC} + \overline{AC} - \overline{AB}}{2w},$$

and

$$F_{32} = \frac{\overline{BC} + \overline{AC} - \overline{AB}}{4w \cos \theta}.$$

C. Radiosity Equations for a Wedge

Facets 1a and 2 are illuminated and have initial emission terms:

$$E_{1a} = \rho_1 E_0 \cos\left(\frac{\pi}{2} - \theta_0 + \theta\right), \text{ if } \left|\frac{\pi}{2} - \theta_0 + \theta\right| < \frac{\pi}{2}$$

$$E_2 = \rho_2 E_0 \cos\left(\frac{\pi}{2} - \theta_0 + \theta\right), \text{ if } \left|\frac{\pi}{2} - \theta_0 + \theta\right| < \frac{\pi}{2}$$

where ρ_1 is the reflectance of slope 1, and ρ_2 is the reflectance of slope 2. E_0 is the total incident solar power per unit area in $[Wm^{-2}]$.

The radiosity equations for the three facets can then be written as:

$$B_{1a} = E_{1a} + \rho_1 [F_{1a2} B_2 + F_{1a3} B_{sky}],$$

$$B_{1b} = \rho_1 [F_{1a2} B_2 + F_{1b3} B_{sky}],$$

and

$$B_2 = E_2 + \rho_2 [F_{21a} B_{1a} + F_{21b} B_{1b} + F_{23} B_{sky}].$$

We have included the contributions from sky light (B_{sky}) in these formulas, but we have set the term to zero for our calculations. The above equations can be solved iteratively, and the convergence criterion is met when the root mean square error Δ of successive iterations ($i+1$) and (i) reaches a lower limit ϵ :

$$\Delta^{(i+1)} = \sqrt{\frac{1}{3}[(B_{1a}^{(i+1)} - B_{1a}^{(i)})^2 + (B_{1b}^{(i+1)} - B_{1b}^{(i)})^2 + (B_2^{(i+1)} - B_2^{(i)})^2]},$$

for $i = 1, 2, 3, \dots$

Note that the following weighted sums of view factors add up to unity :

$$F_{1a2}(1 - f_p) + F_{1b2}f_p + F_{1a3}(1 - f_p) + F_{1b3}f_p = 1,$$

$$F_{21a} + F_{21b} + F_{23} = 1,$$

and

$$F_{31a} + F_{31b} + F_{32} = 1.$$

D. BRF of a Wedge

To compute the BRF from the radiosities, we need to compute the visibility of each facet from a given view direction θ_v that is defined as the counter clockwise angle measured from the x axis. The BRF is then given in general by [8]:

$$\rho_{radiosity}(\theta_0; \theta_v) = \frac{P_{1a}B_{1a} + P_{1b}B_{1b} + P_2B_2}{E_0}.$$

The visibilities P_i for each facet depend on the slope and viewing angle and can be written as:

$$P_{1a} = \begin{cases} 1 & 0 < \theta_v < \theta_c \\ \frac{1-f_p}{1-f_v} & \theta_c < \theta_v < \theta \\ \frac{1-f_p}{2} \left[1 + \frac{\tan \theta}{\tan \theta_v} \right] & \theta < \theta_v < \pi - \theta \\ 0 & \pi - \theta < \theta_v < \pi \end{cases},$$

$$P_{1b} = \begin{cases} 0 & 0 < \theta_v < \theta_c \\ \frac{f_p-f_v}{1-f_v} & \theta_c < \theta_v < \theta \\ \frac{f_p}{2} \left[1 + \frac{\tan \theta}{\tan \theta_v} \right] & \theta < \theta_v < \pi - \theta \\ 0 & \pi - \theta < \theta_v < \pi \end{cases},$$

and

$$P_2 = \begin{cases} 0 & 0 < \theta_v < \theta \\ \frac{1}{2} \left[1 - \frac{\tan \theta}{\tan \theta_v} \right] & \theta < \theta_v < \pi - \theta \\ 1 & \pi - \theta < \theta_v < \pi \end{cases}.$$

The angle θ_c is given by:

$$\theta_c = \tan^{-1} \left[\frac{C_y - S_y}{C_x - S_x} \right].$$

The variable f_v is given by :

$$f_v = \begin{cases} \frac{\sin \theta \cos \theta_v - \cos \theta \sin \theta_v}{\sin \theta} & 0 < \theta_v < \theta \\ 1 - \frac{-\sin \theta \cos \theta_v - \cos \theta \sin \theta_v}{\sin \theta} & \pi - \theta < \theta_v < \pi \end{cases}.$$

The projection of the ray from the observer onto the wedge is the:

$$\vec{V} = \begin{cases} (\vec{A} - \vec{B})f_v & 0 < \theta_v < \theta \\ (\vec{C} - \vec{B})f_v & \pi - \theta < \theta_v < \pi \end{cases}.$$

The sum of the visibilities is equal to unity for all view angles from 0 to π .

The BRF of a wedge, neglecting multiple reflections between the facets, is given by:

$$\rho_{single}(\theta_0; \theta_v) = \frac{P_{1a}E_{1a} + P_{1b}E_{1b} + P_2E_2}{E_0}.$$

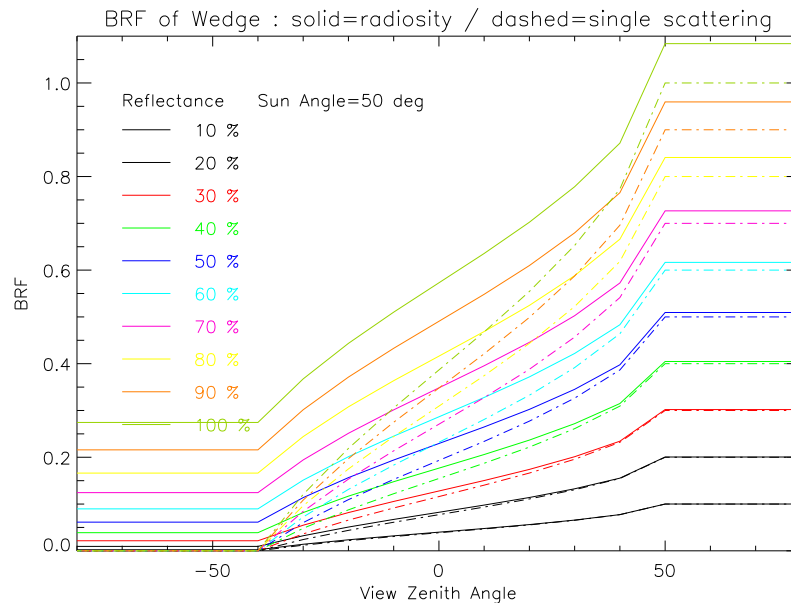


Fig. 9. BRF of a wedge with a slope angle $\theta = 50^\circ$ and a sun angle of $\theta_0 = 40^\circ$

E. Results

The simple wedge model yields some interesting results that seem at first not correct but can be explained. For example if we compute the BRF for a wedge with a slope angle $\theta = 50^\circ$ and a sun angle of $\theta_0 = 40^\circ$, we get the BRF shown in Figure 9. The radiosity computed BRF for viewing zenith angles greater than 50° is larger than unity. How can this be? First, we note that the light is perpendicularly incident on facet 1, thus, the reflectance in the single scattering case must be equal to unity. Second, we note the shaded facet 2 when viewed at angles less than -40° is completely dark for the single scattering case but has a BRF of 0.2744 for a 100 % reflecting surface. Third, we note the view factor from facet 1a to facet 2 is $F_{1a2} = 0.3064$. Fourth, the amount of light facet 1b receives from facet 2 is given by $F_{1a2}B_2 = 0.3064 \cdot 0.2744 = 0.0840$, which must be added to the single scattering term. Thus, we have shown that the BRF for this case can indeed be larger than unity.

From Figure 9, one can see the effect of scattering of light from the adjacent facet is greatest in the shadowed region ($\theta_v < -40^\circ$), this is consistent with the results of other studies.

VII. CONCLUSIONS

The extended radiosity method has been used to compute point spread functions for a layered atmosphere above a heterogeneous ground cover. The adjacency blurring effect was simulated for a scene containing vegetated surfaces, bare soil, and water surfaces. The adjacency PSF is rotationally symmetric for Lambertian surfaces and a nadir view. For non-Lambertian surfaces the PSF is not rotationally symmetric. We have simulated the adjacency effect using computationally efficient filter functions rather than a time Monte Carlo simulation. To illustrate the surface adjacency effect we propose a simple wedge model. The model describes how the reflectance changes as a function of view zenith angle. The model also shows that the BRDF of a surface can change dramatically due to multiple reflections for certain illumination and observation angles.

REFERENCES

- [1] Atmospheric CoRrection Now (ACORN), <http://www.imspec.com/>.
- [2] Gail P. Anderson, Gerald W. Felde, Michael L. Hoke, Anthony J. Ratkowski, Thomas W. Cooley, James H. Chetwynd, Jr., J. A. Gardner, Steven M. Adler-Golden, Michael W. Matthew, Alexander Berk, Lawrence S. Bernstein, Prabhat K. Acharya, David P. Miller, Paul E. Lewis MODTRAN4-based atmospheric correction algorithm: FLAASH (fast line-of-sight atmospheric analysis of spectral hypercubes *Proceedings of SPIE, Algorithms and Technologies for Multispectral, Hyperspectral, and Ultraspectral Imagery VIII*, Vol. 4725, 2003.
- [3] G. Asrar (ed), *Theory and applications of optical remote sensing*, John Wiley & Sons, p. 734, 1989.
- [4] B. Ben Dor, A.D. Devir, G. Shaviv, P. Brusciaglioni, P. Donelli and A. Ismaelli, "Atmospheric scattering effect on spatial resolution of imaging systems," *J. Opt. Soc. Am A*, Vol. 14, No. 6, pp. 1329-1337, 1997.

- [5] A. Berk, G. P. Anderson, L. S. Bernstein, P. K. Acharya, H. Dothe, M. W. Matthew, S. M. Adler-Golden, J. H. Chetwynd, Jr., S. C. Richtsmeier, B. Pukall, C. L. Allred, L. S. Jeong, and M. L. Hoke "MODTRAN4 Radiative Transfer Modeling for Atmospheric Correction," *SPIE Proceeding, Optical Spectroscopic Techniques and Instrumentation for Atmospheric and Space Research III*, Volume 3756, July 1999.
- [6] C.C. Borel, S.A.W. Gerstl, "Simulation of partially obscured scenes using the radiosity method," *SPIE Vol. 1486*, pp.271-277, April 1991.
- [7] C.C. Borel, S.A.W. Gerstl, "Atmospheric corrections using the volume radiosity method," *Proc. Int. Geoscience and Remote Sensing Symposium*, May 26-29, 1992, Houston, Texas, 1992.
- [8] C.C. Borel and S.A.W. Gerstl, "Nonlinear spectral mixing models for vegetative and soil surfaces," *Remote Sensing of Environment*, 47:403-416, 1994.
- [9] P. Chervet, C. Lavigne, A. Roblin and P. Bruscalioni, "Effects of aerosol scattering phase function formulation on point-spread-function calculations," *Applied Optics*, Vol. 41, No.30, pp.6489-6498, 2002.
- [10] D.J. Diner and J.V. Martonchik, "Atmospheric transmittance from spacecraft using multiple view angle imagery," *Applied Optics*, 24:21, pp.3503-3511, 1985.
- [11] A.F.H. Goetz, B.C. Kindel, M. Ferri and Z. Qu, "The high-accuracy atmospheric correction for hyperspectral data (HATCH) model," *IEEE TGARS*, Vol.41, No. 6, pp. 1223-1231, 2003.
- [12] B. Hapke, "Bidirectional reflectance spectroscopy: 1. theory," *J. Geophys. Res.*, Vol. 86, No. B4, pp. 3039-3054, April, 1981.
- [13] H.C. Hottel and A.F. Sarofim. *Radiative Transfer*. McGraw-Hill Book Company, New York, New York, 1967.
- [14] Y.J. Kaufman, "Atmospheric effects on remote sensing of surface reflectance," *SPIE proceedings*, 475:20-33, 1984.
- [15] K.-N. Liou, *An introduction to atmospheric radiation*. Academic Press, Orlando, FL, 1980.
- [16] M.W. Matthew, S.M. Adler-Golden, A. Berk, S.C. Richtsmeier, R.Y. Levine, L.S. Bernstein, P.K. Acharya, G.P. Anderson, G.W. Felde, M.P. Hoke, A. Ratkowski, H. Burke, R.D. Kaiser, and D.P. Miller, "Status of Atmospheric Correction Using a MODTRAN4-based Algorithm," *SPIE Proceeding, Algorithms for Multispectral, Hyperspectral, and Ultraspectral Imagery VI*, Volume 4049, 2000.
- [17] C. Miesch, X. Briottet, Y.H. Kerr and F. Cabot, "Radiative Transfer solution for rugged and heterogeneous scene observations," *Applied Optics*, Vol. 39, No. 36, pp.6830-6846, 2000.
- [18] William H. Press, Brian P. Flannery, Saul A. Teukolsky, William T. Vetterling "Numerical Recipes in FORTRAN," Cambridge University Press; 2 edition (January 15, 1992).
- [19] P.N. Reinersmann and K.L. Carder, "Monte Carlo simulation of the atmospheric point-spread function with an application to correction for the adjacency effect," *Applied Optics*, Vol. 4, No. 21, pp.4453- 4471, 1995.
- [20] R. Richter, "A fast atmospheric correction algorithm applied to Landsat TM images," *Int. J. Remote Sensing*, 11, pp.159-166, 1990.
- [21] R. Richter, D. Schlapfer "Geo-atmospheric processing of wide-FOV airborne imaging spectrometry data," *Proceedings of SPIE Volume, Remote Sensing for Environmental Monitoring, GIS Applications, and Geology*, Vol. 4545, 2003.
- [22] H.E. Rushmeier and K.E. Torrance. "The zonal method for calculating light intensities in the presence of a participating medium," *SIGGRAPH Proceedings*, 21(4):293, July 1987.
- [23] D. Tanré, M. Herman and P.Y. Deschamps, "Influence of the background contribution upon space measurements of ground reflectance," *Applied Optics*, 20:20, pp.3676-3684, 1981.
- [24] W.A. Pearce, "A study of the effects of the atmosphere on thematic mapper observations," *Report 004-77, EG&G*, Washington Anal. Serv. Center, Riverdale, MD, 1977.
- [25] B. Pinty, M. Verstraete and R. Dickinson, "A physical model of the bidirectional reflectance of vegetation canopies: 2. inversion and validation," *J. Geophys. Res.*, Vol.95, No. D8, pp.11767-11775, 1990.
- [26] R.J. Woodham and T.K. Lee, "Photometric method for radiometric correction of multispectral scanner data," *Canadian Journal of Remote Sensing*, Vol.11, No.2, December 1985.